ACS APPLIED MATERIALS & INTERFACES

www.acsami.org Research Article

Tailoring the d-Band Center of Double-Perovskite $LaCo_xNi_{1-x}O_3$ Nanorods for High Activity in Artificial N_2 Fixation

Kaibin Chu, Michiel De Ras, Dewei Rao, Johan A. Martens, Johan Hofkens, Feili Lai,* and Tianxi Liu*

Cite This: ACS Appl. Mater. Interfaces 2021, 13, 13347−13353 Read Online

ACCESS | Metrics & More | Article Recommendations | Supporting Information

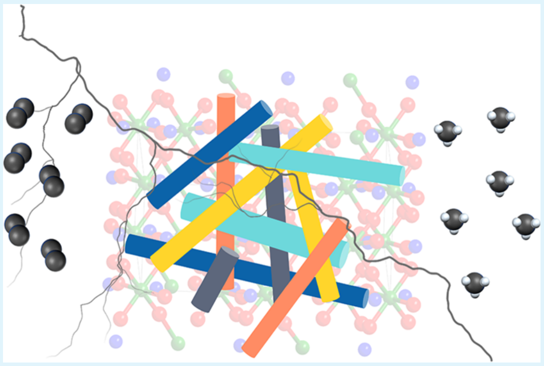

ABSTRACT: The d-band center of a catalyst can be applied for the prediction of its catalytic activity, but the application of d-band theory for the electrocatalytic nitrogen reduction reaction (eNRR) has rarely been studied in perovskite materials. In this work, a series of double-perovskite $LaCo_xNi_{1-x}O_3$ (LCNO) nanorods (NRs) were synthesized as models, where the d-band centers can be modulated by changing the stoichiometric ratios between Co and Ni elements. Experimentally, the LCNO-III NRs (x = 0.5) attained the highest faradic efficiency and NH_3 yield rate among various LCNO NRs. This result matches well with the finding from theoretical calculations that LCNO-III has the most positive d-band center ($\varepsilon_d = -0.96$ eV vs Fermi level), thus confirming that LCNO-III shows the strongest adsorption ability for N_2 molecules (adsorption energy value of −2.01 eV) for the subsequent N_2 activation and reduction reactions. Therefore, this work proposes a general rule to adopt for developing novel catalysts (especially perovskite-based catalysts) for substantially increasing the eNRR activity by modulating the corresponding d-band centers.

KEYWORDS: *La-based perovskite, d-band center, electrocatalysis, ammonia, nitrogen reduction reaction*

1. INTRODUCTION

Ammonia (NH_3) is a typical high-hydrogen energy carrier with zero carbon (17.6% hydrogen by mass); it is used as a propellant in rockets and missiles[1] and plays a crucial role in producing chemicals (e.g., nitric acid and urea).[2] Currently, the well-known Haber−Bosch process (HBP) is still the mainstream method to produce ammonia in the chemical industry, and this process relies heavily on harsh conditions (200−250 bar, 400−500 °C),[3,4] resulting in significant energy consumption and environmental pollution. As a much greener and milder strategy than the HBP, the electrocatalytic nitrogen reduction reaction (eNRR) offers an attractive route to achieve the conversion from N_2 resources to NH_3 production. To accelerate the dissociation of inert N_2 molecules and reduce the energy barrier during the eNRR process, high-efficiency catalysts are urgently needed. Recently, investigations of eNRR catalysts have focused on metals,[5] metal oxides,[6,7] metal nitrides or carbides,[8,9] metal complexes,[10−12] and other metal-free materials,[13] among which noble-metal-based catalysts[14−17] are regarded as the most promising electrocatalysts for nitrogen reduction with high NH_3 yields. However, the limited reserves and high cost of noble metals hinder their large-scale applications. As great candidates for eNRR electrocatalysts, perovskite oxide materials have been studied by various approaches in recent years, such as $LaCoO_3$, $LaCrO_3$, $LaFeO_3$, $La_2Ti_2O_7$, and $Ce_{1/3}NbO_3$.[18−24]

Recently, ABO_3-type double perovskites, where the A-site represents rare-earth or alkali metal cations and B-sites are transition-metal cations, have attracted considerable attention for various energy-related applications because of their structural tunability and high electronic and ionic conductivity.[25−27] The electrocatalytic performance of perovskite oxides can be effectively improved by some methods (such as oxygen vacancy engineering and manipulating the induced synergetic effects).[28,29] Inspired by the recent work in which La atoms in La_2O_3 behave as active sites for efficiently adsorbing N_2,[30] the electrochemical properties of ABO_3-type double perovskites may be easily controlled by the partial substitution of B-site cations, as the B-site of perovskites is generally regarded as the active center for electrocatalysis.[31] For example, Tong et al. reported a superexchange effect by developing a series of double-perovskite La_2NiMnO_6 compounds with different particle sizes. The La_2NiMnO_6 nanoparticle measuring 33 nm shows the best oxygen evolution reaction (OER) performance in alkaline media, which benefits from optimizing the e_g electron filling state and accelerating the formation of

Received: January 23, 2021
Accepted: February 26, 2021
Published: March 10, 2021

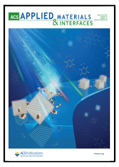

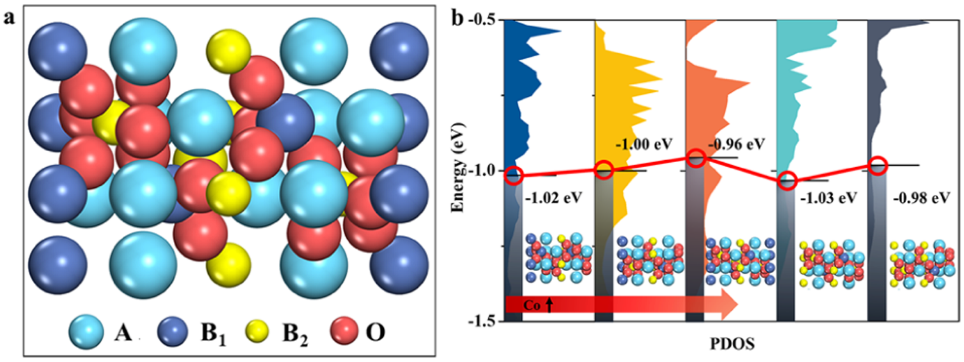

Figure 1. (a) Model of La-based ABO_3-type perovskite. (b) Calculated PDOS and d-band center values of Co for LCNO perovskites. The light blue, yellow, blue, and red balls represent La, Co, Ni, and O atoms, respectively.

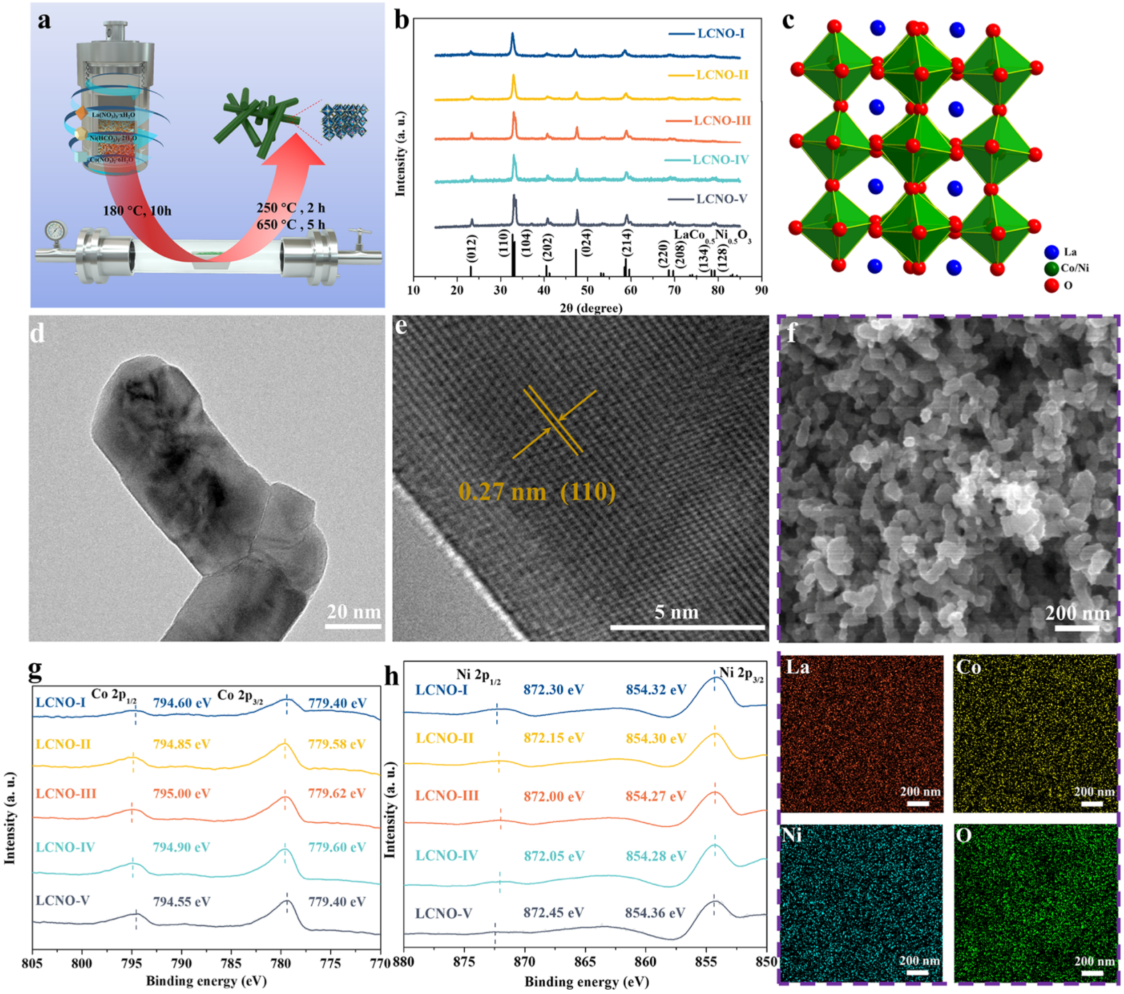

Figure 2. (a) Schematic illustration of the synthetic procedure for LCNO NRs. (b) X-ray diffraction (XRD) patterns of LCNO-I, LCNO-II, LCNO-III, LCNO-IV, and LCNO-V. (c) Crystal model of LCNO NRs. (d) Transmission electron microscopy (TEM) and (e) high-resolution-TEM (HRTEM) images of LCNO-III NRs. (f) Scanning electron microscopy (SEM) image and the corresponding energy dispersive spectroscopy (EDS) elemental mappings for LCNO-III. XPS spectra of (g) Co 2p and (h) Ni 2p for LCNO-I, LCNO-II, LCNO-III, LCNO-IV, and LCNO-V.

the active species of the electrocatalyst surface.[32] One of the main research highlights of ABO_3-type double perovskites is the variability of the stoichiometric ratio between B_1 and B_2 cations (here, B_1 and B_2 are two possible cations in the B-site), which is closely related to the electronic structures of perovskites, such as the charge density distribution, d-band center, and electronic conductivity. That is, the surface environment and catalytic activity of ABO_3-type double perovskites can be easily modulated by searching for the most suitable stoichiometric ratio between B_1 and B_2 cations; however, this possible effect has not yet been studied in the eNRR field.

Herein, La-based ABO_3-type ($A = La$, $B_1 = Co$, $B_2 = Ni$) perovskite was chosen as a model (Figure 1a), where the stoichiometric ratio between B_1 and B_2 cations is randomly selected. In particular, five $LaCo_xNi_{1-x}O_3$ ($x = 0.2, 0.33, 0.5,$

https://dx.doi.org/10.1021/acsami.1c01510

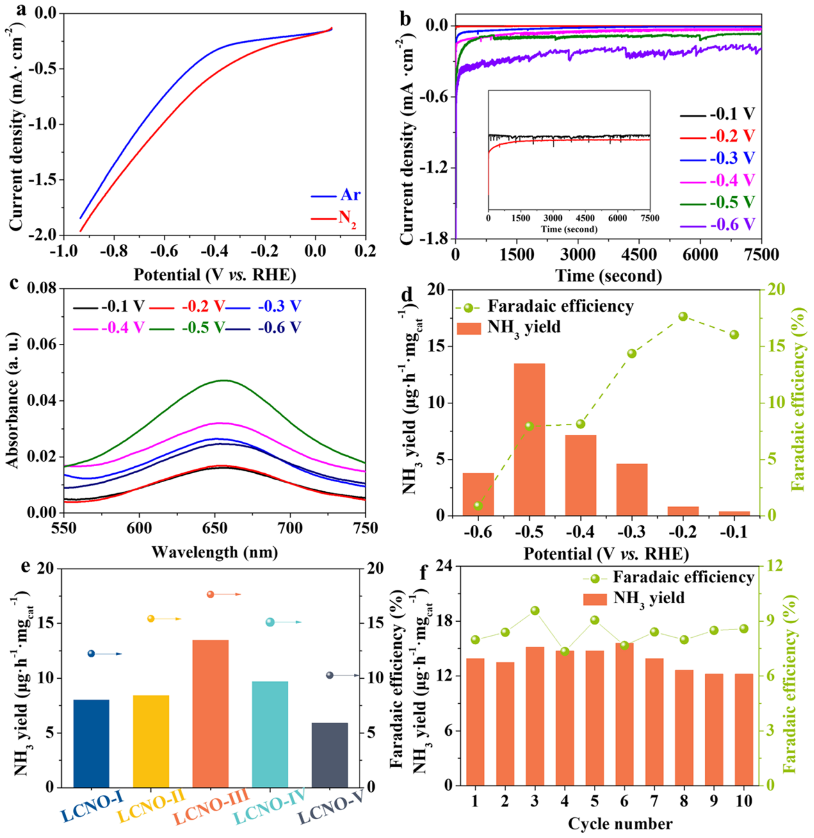

Figure 3. (a) LSV curves of LCNO-III recorded in electrolytes with different conditions. (b) Time-dependent current density curves of LCNO-III under various potentials in nitrogen-saturated 0.1 M Na_2SO_4 electrolyte. (c) UV−vis absorption spectra of the electrolytes (after working 7500 s) stained with indophenol indicator at various potentials. (d) NH_3 yield and faradic efficiency over LCNO-III at various potentials. (e) NH_3 yield and FE of different electrodes at a potential of −0.5 V. (f) Cycling test of LCNO-III at −0.5 V.

0.67, and 0.8) models were constructed and denoted as LCNO-I, LCNO-II, LCNO-III, LCNO-IV, and LCNO-V, respectively. According to the partial density of state (PDOS) for Co elements shown in Figure 1b, LCNO-III displays the most positive d-band center (ε_d = −0.96 eV) with the closest distance to the Fermi level, which suggests that it may have the highest interaction with the adsorbate (e.g., N_2) among the five models. From an experimental perspective, we also fabricated a series of LCNO nanorods (NRs) with the same stoichiometric ratios as those used in the five theoretical models to check the above result with density functional theory (DFT) calculations and determine whether it is possible to optimize the eNRR property of LCNO by simply controlling the stoichiometric ratio. LCNO NRs with small diameters were obtained by a facile coprecipitation method with three steps, as shown in Figure 2a. Initially, $La(NO_3)_3 \cdot xH_2O$, $Ni(HCO_2)_2 \cdot 2H_2O$, and $Co(NO_3)_2 \cdot 6H_2O$ were well mixed in water with certain stoichiometric ratios. After adding a certain amount of KOH solution, the suspension was heated to 180 °C and maintained for 10 h. Finally, the powder obtained was calcined at 250 and 650 °C successively. More details of the LCNO synthesis can be found in the Experimental Section of the Supporting Information.

2. RESULTS AND DISCUSSION

The crystal structures of the LCNO NRs were first characterized by powder X-ray diffraction (PXRD). In Figure 2b, the XRD patterns of the different LCNO NRs are in agreement with the rhombohedral structure of $LaCo_{0.5}Ni_{0.5}O_3$ (JCPDS No. 58-0834), where the diffraction peaks at 23.1, 32.7, 33.2, 40.5, 47.3, 58.8, 68.6, 69.7, 78.4, and 79.1° can be indexed to the (012), (110), (104), (202), (024), (214), (220), (208), (134), and (128) planes, respectively. Notably, with increasing Ni, the diffraction peak for the (110) plane shifts to a lower angle direction (Figure S1), and this is because of the larger covalent radius of Ni^{3+} than that of Co^{3+}.[33] LCNO NRs have an ABO_3 perovskite structure, in which the lanthanum cations occupy the cavities between edge-sharing MO_6 (M = Co or Ni) octahedra (Figure 2c). The metal−oxygen bond of perovskites can be utilized to tune their electronic structures and control their surface-binding energetic properties.[34]

The morphology images of LCNO NRs (Figures 2d, S2, and S3) demonstrate that the LCNO perovskites consist of thousands of NRs with diameters of ∼70 nm. As observed in Figures 2e and S3, all of the LCNO perovskites display a *d*-spacing of 0.27 nm that can be assigned to the (110) plane. This indicates that the (110) plane is the dominant crystal plane in all LCNO perovskites, and this plane is also chosen as the crystal surface in the following theoretical calculations for nitrogen adsorption. Figure 2f displays the energy-dispersive X-ray spectroscopy (EDS) results for LCNO-III, indicating La, Co, Ni, and O elements in LCNO-III NRs with uniform distributions. The molar ratios of Co:Ni were confirmed by combining the EDS spectrum and inductively coupled plasma-optical emission spectra (ICP-OES), as shown in Figure S4; the results indicate that the measured ratios of various LCNO NRs are very close to the theoretical ratios.

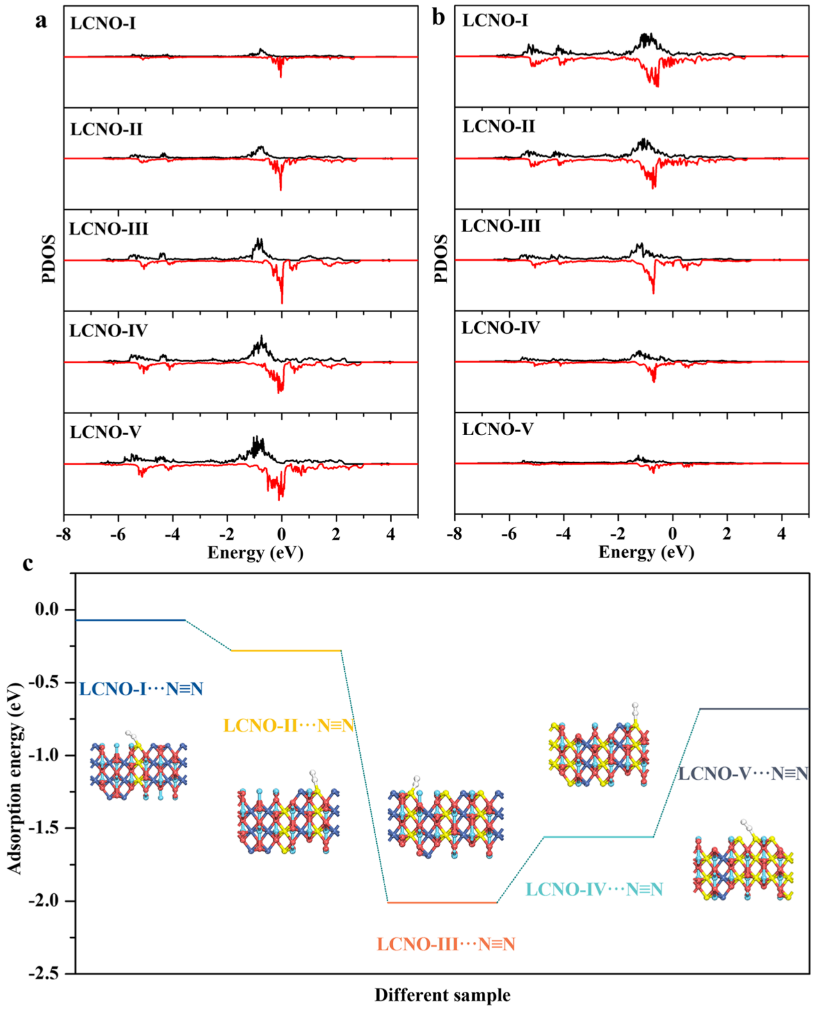

Figure 4. Calculated PDOS of (a) Co and (b) Ni for various LCNO perovskites. (c) Adsorption free energy of N_2 molecules on the (110) surfaces for various LCNO perovskites.

To investigate the possible change in the electronic structure for various LCNO NRs, their chemical states and surface compositions were investigated by X-ray photoelectron spectroscopy (XPS) measurements. Only La, Co, Ni, and O elements are discerned without any detected signal from the N element (Figures S5 and S6), excluding the interference of a nitrogen source from the electrocatalyst itself during the following eNRR process. The core-level spectra of Co 2p and Ni 2p for all samples are displayed in Figure 2g,h. As the ratio of Co/Ni increases from 0.25 to 1.0, the Co $2p_{1/2}$ and Co $2p_{3/2}$ peaks of LCNO NRs move to more positive binding energies. Subsequently, with the increasing ratio of Co/Ni from 1.0 to 4.0, the Co 2p peaks return to relatively negative binding energies. However, the Ni 2p peaks show an opposite trend (Figure 2h). That is, the electronic structure of LCNO could be well modulated by controlling the ratio of Co/Ni. The electrons belonging to Co atoms would be partially delocalized to neighboring atoms with the incorporation of Ni in the LCNO perovskite. LCNO-III NRs show the most obvious electronic delocalization among the five samples, indicating that there may be thousands of active regions in LCNO-III NRs for N_2 coupling and activation.

The eNRR activities of LCNO NRs were evaluated using a typical three-electrode system (more details are provided in the Supporting Information). Linear sweep voltammetry (LSV) curves were collected to preliminarily estimate the potential windows for electrosynthesis. As shown in Figures 3a and S7, when the potential decreases from −0.10 V vs reversible hydrogen electrode (RHE), the current density in the nitrogen-saturated electrolyte is higher than that in the argon-saturated electrolyte, implying that an appropriate potential window for the eNRR of LCNO NRs would be between −0.10 V vs RHE and −0.60 V vs RHE. The quantities of ammonia (NH_3) and hydrazine (N_2H_4) were determined by the UV method. The standard curves are displayed in Figures S8 and S9. As shown in Figures 3b and S10 for the current density curves of various LCNO NRs, there was no significant change in current density at various potentials, demonstrating the good durability of LCNO NRs. The UV−vis absorption spectra for the electrolytes stained with the indophenol indicator after 7500 s of eNRR are provided in Figures 3c and S11. As observed, the electrolyte at −0.5 V vs RHE shows the maximum absorbance intensity at 655 nm. It is indicated that this potential is the most suitable one to increase the NH_3 yield rate. Furthermore, both the NH_3 formation rate and faradic efficiency (FE) are plotted in Figures 3d,e and S12. For LCNO-III NRs, the maximum NH_3 yield is obtained at −0.50 V vs RHE (13.48 μg h^{-1} mg^{-1}_{cat}). As the potential increases from −0.50 to −0.60 V vs RHE and decreases from −0.5 to −0.1 V vs RHE, the NH_3 yield decreases dramatically, probably due to the competitive hydrogen evolution reaction on the LCNO-loaded electrode surface.[35,36] The highest FE for LCNO-III NRs is 17.65% when the potential is fixed at −0.2 V vs RHE. Notably, LCNO-III NRs display the highest NH_3 yield and FE among the various LCNO NRs (Figure 3e), and these values are even superior to some previously reported aqueous-based eNRR electrocatalysts and are comparable to other perovskite oxide catalysts (Table S1). The excellent reusability of LCNO-III NRs was further evaluated by recycling electrolysis at −0.50 V vs RHE. As shown in Figures 3f and S13a, LCNO-III has negligible changes in both FE and NH_3 yield, suggesting that LCNO-III exhibits highly stable and repeatable eNRR performance during the stability tests. This can also be proven from the chronoamperometry curve of LCNO-III (Figure S13b), in which there are no obvious fluctuations in the current density after 10 cycles. Notably, no obvious amount of the byproduct of N_2H_4 could be detected at different given potentials (Figure S14a−e), suggesting that all of the LCNO NRs have excellent selectivity for N_2−NH_3 conversion.

In addition, some comparative experiments were performed to confirm whether the NH_3 detected was generated from the eNRR process on LCNO NRs instead of from an impurity: (1) pristine carbon paper electrode was tested as the working electrode under a nitrogen-saturated atmosphere; (2) LCNO-III was tested in an argon-saturated electrolyte at −0.50 V vs RHE; (3) LCNO-III was tested in a nitrogen-saturated electrolyte at open-circuit potential; and (4) the concentration of NH_3 in a 0.1 M Na_2SO_4 solution was measured after purging with N_2 for 7500 s. Clearly, the poorly responsive UV−vis absorption spectra in Figure S15 suggest that almost no NH_3 could be detected in either case. That is, the detected NH_3 was produced from N_2 sources by LCNO NRs via the eNRR process. We also conducted a ^{15}N isotope labeling experiment to verify this hypothesis. The ^1H NMR spectrum of LCNO-III for $^{15}N_2$ is shown in Figure S16; no signal from $^{14}NH_4^+$ is detected in the region of 6.85−7.15 ppm, indicating that ammonia is produced by the eNRR instead of by other contaminants.

To gain further insight into the enhanced eNRR performance of LCNO-III and its electronic structure, DFT calculations were conducted again. As shown in Figure 1b, LCNO-III has the most positive ε_d value (ε_d = −0.96 eV) among the various LCNO perovskites, which indirectly reveals that it has the strongest binding ability for the reactant. However, there is still a question that remains to be answered: Is cobalt or nickel the adsorption site for nitrogen molecules during the eNRR process? As shown in Figure 4a,b, the cobalt atoms exhibit an obviously enhanced PDOS approaching the Fermi level with respect to those of nickel atoms. Moreover, we found that the ε_d values of cobalt atoms for all LCNO perovskites are much closer to the Fermi level than those of nickel (Figure S17). Taking these two results into consideration, cobalt is more likely to be the active site for the eNRR process. Generally, the adsorption of nitrogen molecules on the surface of eNRR catalysts can be one of the most important steps for the whole eNRR pathway.[37] Therefore, the adsorption energy values of N_2 molecules on the (110) surface of different LCNO perovskites were calculated, where cobalt atoms were optimized as the adsorption sites. As shown in Figure 4c, LCNO-III has the lowest adsorption energy value for N_2 molecules (−2.01 eV) compared to those for LCNO-I (−0.07 eV), LCNO-II (−0.28 eV), LCNO-IV (−1.56 eV), and LCNO-V (−0.68 eV), which matches well with the results from the d-band theory.

3. CONCLUSIONS

In conclusion, we designed a new platform (La-based ABO_3-type double perovskite) to study the relationship between the d-band center and eNRR performance systematically. Compared to other LCNO NRs with similar structures but different ratios of Co/Ni, LCNO-III enables effective nitrogen adsorption and subsequent activation, resulting in LCNO-III having the highest eNRR activity (NH_3 yield of 13.48 μg h^{-1} mg_{cat}^{-1} and FE of 17.65%), and robust long-term electrochemical durability. It is also confirmed by the corresponding theoretical calculations that among the LCNO NRs, LCNO-III displays the closest d-band center to the Fermi energy level and the strongest adsorption ability for N_2 molecules at the cobalt site. This study not only offers a favorable earth-abundant catalyst for eNRR but opens a new path for the rational design of La-based perovskites to convert N_2 into NH_3 under the guidance of the d-band theory.

■ ASSOCIATED CONTENT

Supporting Information

The Supporting Information is available free of charge at https://pubs.acs.org/doi/10.1021/acsami.1c01510.

Chemicals, synthesis of perovskite-type $LaCo_xNi_{1-x}O_3$ nanorods (x = 0.2, 0.33, 0.5, 0.67, 0.8), characterization, computational methods, electrochemical measurements, determination of NH_3 and N_2H_4; XRD patterns (Figure S1); SEM images (Figure S2); HRTEM images (Figure S3); atomic ratios (Figure S4); XPS spectra (Figures S5 and S6); LSV curves (Figure S7); UV−vis curves (Figures S8 and S9); chronoamperometry results (Figure S10); UV−vis absorption spectra (Figures S11 and S13−S15); NH_3 yield and faradic efficiency (Figure S12); isotopic labeling results (Figure S16); d-band centers (Figure S17); and comparison of the electrocatalytic NRR performance of $LaCo_{0.5}Ni_{0.5}O_3$ with other aqueous-based NRR electrocatalysts at room temperature (Table S1) (PDF)

■ AUTHOR INFORMATION

Corresponding Authors

Feili Lai − *Department of Chemistry, KU Leuven, Leuven 3001, Belgium*; orcid.org/0000-0002-4945-0737; Email: feili.lai@kuleuven.be

Tianxi Liu − *Key Laboratory of Synthetic and Biological Colloids, Ministry of Education, School of Chemical and Material Engineering, International Joint Research Laboratory for Nano Energy Composites, Jiangnan University, Wuxi 214122, P. R. China*; Email: txliu@jiangnan.edu.cn

Authors

Kaibin Chu − *Key Laboratory of Synthetic and Biological Colloids, Ministry of Education, School of Chemical and Material Engineering, International Joint Research Laboratory for Nano Energy Composites, Jiangnan University, Wuxi 214122, P. R. China*

Michiel De Ras − *Department of Chemistry, KU Leuven, Leuven 3001, Belgium*

Dewei Rao − *School of Materials Science and Engineering, Jiangsu University, Zhenjiang 212013, P. R. China;* orcid.org/0000-0003-0410-5259

Johan A. Martens − *Centre of Surface Chemistry and Catalysis: Characterisation and Application Team, KU Leuven, Leuven 3001, Belgium*

Johan Hofkens − *Department of Chemistry, KU Leuven, Leuven 3001, Belgium; Max Planck Institute for Polymer Research, Mainz 55128, Germany;* orcid.org/0000-0002-9101-0567

Complete contact information is available at: https://pubs.acs.org/10.1021/acsami.1c01510

Notes

The authors declare no competing financial interest.

■ ACKNOWLEDGMENTS

The authors are grateful for the financial support from the National Natural Science Foundation of China (21674019, 51801075), the Shanghai Scientific and Technological Innovation Project (18JC1410600), and the Program of the Shanghai Academic Research Leader (17XD1400100). J.H. and J.A.M. gratefully acknowledge the financial support from the Flemish Government through the Moonshot cSBO project P2C (HBC.2019.0108) and through long-term structural funding (Methusalem CASAS2, Meth/15/04) and from Interne Fondsen KU Leuven through project C3/20/067. D.R. gratefully acknowledges the support from the Jiangsu Overseas Visiting Scholar Program for University Prominent Young and Mid-aged Teachers and Presidents. Theoretical work was carried out at the LvLiang Cloud Computing Center of China, and the calculations were performed on a TianHe-2 system.

■ REFERENCES

(1) Li, J.; He, L.; Liu, X.; Cheng, X.; Li, G. Electrochemical Hydrogenation with Gaseous Ammonia. *Angew. Chem., Int. Ed.* **2019**, *58*, 1759−1763.

(2) Rosca, V.; Duca, M.; de Groot, M. T.; Koper, M. T. M. Nitrogen Cycle Electrocatalysis. *Chem. Rev.* **2009**, *109*, 2209−2244.

(3) Chen, J. G.; Crooks, R. M.; Seefeldt, L. C.; Bren, K. L.; Bullock, R. M.; Darensbourg, M. Y.; Holland, P. L.; Hoffman, B.; Janik, M. J.; Jones, A. K.; Kanatzidis, M. G.; King, P.; Lancaster, K. M.; Lymar, S. V.; Pfromm, P.; Schneider, W. F.; Schrock, R. R. Beyond Fossil Fuel-Driven Nitrogen Transformations. *Science* **2018**, *360*, No. eaar6611.

(4) Mehta, P.; Barboun, P.; Herrera, F. A.; Kim, J.; Rumbach, P.; Go, D. B.; Hicks, J. C.; Schneider, W. F. Overcoming Ammonia Synthesis Scaling Relations with Plasma-Enabled Catalysis. *Nat. Catal.* **2018**, *1*, 269−275.

(5) Li, L.; Tang, C.; Xia, B.; Jin, H.; Zheng, Y.; Qiao, S.-Z. Two-Dimensional Mosaic Bismuth Nanosheets for Highly Selective Ambient Electrocatalytic Nitrogen Reduction. *ACS Catal.* **2019**, *9*, 2902−2908.

(6) Wang, Z.; Gong, F.; Zhang, L.; Wang, R.; Ji, L.; Liu, Q.; Luo, Y.; Guo, H.; Li, Y.; Gao, P.; Shi, X.; Li, B.; Tang, B.; Sun, X. Electrocatalytic Hydrogenation of N_2 to NH_3 by MnO: Experimental and Theoretical Investigations. *Adv. Sci.* **2019**, *6*, No. 1801182.

(7) Lai, F.; Feng, J.; Ye, X.; Zong, W.; He, G.; Yang, C.; Wang, W.; Miao, Y.-E.; Pan, B.; Yan, W.; Liu, T.; Parkin, I. P. Oxygen Vacancy Engineering in Spinel-Structured Nanosheet Wrapped Hollow Polyhedra for Electrochemical Nitrogen Fixation under Ambient Conditions. *J. Mater. Chem. A* **2020**, *8*, 1652−1659.

(8) Zhang, R.; Zhang, Y.; Ren, X.; Cui, G.; Asiri, A. M.; Zheng, B.; Sun, X. High-Efficiency Electrosynthesis of Ammonia with High Selectivity under Ambient Conditions Enabled by VN Nanosheet Array. *ACS Sustainable Chem. Eng.* **2018**, *6*, 9545−9549.

(9) Cheng, H.; Ding, L.-X.; Chen, G.-F.; Zhang, L.; Xue, J.; Wang, H. Molybdenum Carbide Nanodots Enable Efficient Electrocatalytic Nitrogen Fixation under Ambient Conditions. *Adv. Mater.* **2018**, *30*, No. 1803694.

(10) Jeong, E.-Y.; Yoo, C.-Y.; Jung, C. H.; Park, J. H.; Park, Y. C.; Kim, J.-N.; Oh, S.-G.; Woo, Y.; Yoon, H. C. Electrochemical Ammonia Synthesis Mediated by Titanocene Dichloride in Aqueous Electrolytes under Ambient Conditions. *ACS Sustainable Chem. Eng.* **2017**, *5*, 9662−9666.

(11) Lai, F.; Chen, N.; Ye, X.; He, G.; Zong, W.; Holt, K. B.; Pan, B.; Parkin, I. P.; Liu, T.; Chen, R. Refining Energy Levels in ReS_2 Nanosheets by Low-Valent Transition-Metal Doping for Dual-Boosted Electrochemical Ammonia/Hydrogen Production. *Adv. Funct. Mater.* **2020**, *30*, No. 1907376.

(12) Lai, F.; Zong, W.; He, G.; Xu, Y.; Huang, H.; Wen, B.; Rao, D.; Martens, J. A.; Hofkens, J.; Parkin, I. P.; Liu, T. N_2 Electroreduction to NH_3 by Selenium Vacancy-Rich $ReSe_2$ Catalysis at an Abrupt Interface. *Angew. Chem., Int. Ed.* **2020**, *59*, 13320−13327.

(13) Yu, X.; Han, P.; Wei, Z.; Huang, L.; Gu, Z.; Peng, S.; Ma, J.; Zheng, G. Boron-Doped Graphene for Electrocatalytic N_2 Reduction. *Joule* **2018**, *2*, 1610−1622.

(14) Bai, J.; Huang, H.; Li, F.-M.; Zhao, Y.; Chen, P.; Jin, P.-J.; Li, S.-N.; Yao, H.-C.; Zeng, J.-H.; Chen, Y. Glycerol Oxidation Assisted Electrocatalytic Nitrogen Reduction: Ammonia and Glyceraldehyde Co-Production on Bimetallic RhCu Ultrathin Nanoflake Nano-aggregates. *J. Mater. Chem. A* **2019**, *7*, 21149−21156.

(15) Li, S.-J.; Bao, D.; Shi, M.-M.; Wulan, B.-R.; Yan, J.-M.; Jiang, Q. Amorphizing of Au Nanoparticles by CeO_x-RGO Hybrid Support towards Highly Efficient Electrocatalyst for N_2 Reduction under Ambient Conditions. *Adv. Mater.* **2017**, *29*, No. 1700001.

(16) Shi, M.-M.; Bao, D.; Wulan, B.-R.; Li, Y.-H.; Zhang, Y.-F.; Yan, J.-M.; Jiang, Q. Au Sub-Nanoclusters on TiO_2 toward Highly Efficient and Selective Electrocatalyst for N_2 Conversion to NH_3 at Ambient Conditions. *Adv. Mater.* **2017**, *29*, No. 1606550.

(17) Pang, F.; Wang, Z.; Zhang, K.; He, J.; Zhang, W.; Guo, C.; Ding, Y. Bimodal Nanoporous Pd_3Cu_1 Alloy with Restrained Hydrogen Evolution for Stable and High Yield Electrochemical Nitrogen Reduction. *Nano Energy* **2019**, *58*, 834−841.

(18) Zhang, S.; Duan, G.; Qiao, L.; Tang, Y.; Chen, Y.; Sun, Y.; Wan, P.; Zhang, S. Electrochemical Ammonia Synthesis from N_2 and H_2O Catalyzed by Doped $LaFeO_3$ Perovskite under Mild Conditions. *Ind. Eng. Chem. Res.* **2019**, *58*, 8935−8939.

(19) Ohrelius, M.; Guo, H.; Xian, H.; Yu, G.; Alshehri, A. A.; Alzahrani, K. A.; Li, T.; Andersson, M. Electrochemical Synthesis of Ammonia Based on a Perovskite $LaCrO_3$ Catalyst. *ChemCatChem* **2020**, *12*, 731−735.

(20) Li, C.; Ma, D.; Mou, S.; Luo, Y.; Ma, B.; Lu, S.; Cui, G.; Li, Q.; Liu, Q.; Sun, X. Porous $LaFeO_3$ Nanofiber with Oxygen Vacancies as an Efficient Electrocatalyst for N_2 Conversion to NH_3 under Ambient Conditions. *J. Energy Chem.* **2020**, *50*, 402−408.

(21) Yu, J.; Li, C.; Li, B.; Zhu, X.; Zhang, R.; Ji, L.; Tang, D.; Asiri, A. M.; Sun, X.; Li, Q.; Liu, S.; Luo, Y. A Perovskite $La_2Ti_2O_7$ Nanosheet as an Efficient Electrocatalyst for Artificial N_2 Fixation to NH_3 in Acidic Media. *Chem. Commun.* **2019**, *55*, 6401−6404.

(22) Hu, X.; Sun, Y.; Guo, S.; Sun, J.; Fu, Y.; Chen, S.; Zhang, S.; Zhu, J. Identifying Electrocatalytic Activity and Mechanism of $Ce_{1/3}NbO_3$ Perovskite for Nitrogen Reduction to Ammonia at Ambient Conditions. *Appl. Catal., B* **2021**, *280*, No. 119419.

(23) Liu, Y.; Kong, X.; Guo, X.; Li, Q.; Ke, J.; Wang, R.; Li, Q.; Geng, Z.; Zeng, J. Enhanced N_2 Electroreduction over $LaCoO_3$ by Introducing Oxygen Vacancies. *ACS Catal.* **2020**, *10*, 1077−1085.

(24) Chu, K.; Liu, F.; Zhu, J.; Fu, H.; Zhu, H.; Zhu, Y.; Zhang, Y.; Lai, F.; Liu, T. A General Strategy to Boost Electrocatalytic Nitrogen Reduction on Perovskite Oxides via the Oxygen Vacancies Derived from A-Site Deficiency. *Adv. Energy. Mater.* **2021**, *11*, No. 2003799.

(25) Shao, Z.; Haile, S. M. A High-Performance Cathode for the Next Generation of Solid-Oxide Fuel Cells. *Nature* **2004**, *431*, 170−173.

(26) Suntivich, J.; Gasteiger, H. A.; Yabuuchi, N.; Nakanishi, H.; Goodenough, J. B.; Shao-Horn, Y. Design Principles for Oxygen-Reduction Activity on Perovskite Oxide Catalysts for Fuel Cells and Metal-Air Batteries. *Nat. Chem.* **2011**, *3*, 546−550.

(27) Sengodan, S.; Choi, S.; Jun, A.; Shin, T. H.; Ju, Y.-W.; Jeong, H. Y.; Shin, J.; Irvine, J. T. S.; Kim, G. Layered Oxygen-Deficient Double Perovskite as an Efficient and Stable Anode for Direct Hydrocarbon Solid Oxide Fuel Cells. *Nat. Mater.* **2015**, *14*, 205−209.

(28) Dai, J.; Zhu, Y.; Tahini, H.; Lin, Q.; Chen, Y.; Guan, D.; Zhou, C.; Hu, Z.; Lin, H.; Chan, T.; Chen, C.; Smith, S.; Wang, H.; Zhou, W.; Shao, Z. Single-Phase Perovskite Oxide with Super-Exchange induced Atomic-Scale Synergistic Active Centers Enables Ultrafast Hydrogen Evolution. *Nat. Commun.* **2020**, *11*, No. 5657.

(29) Zhu, Y.; Lin, Q.; Zhong, Y.; Tahini, H.; Shao, Z.; Wang, H. Metal Oxide-Based Materials as an Emerging Family of Hydrogen Evolution Electrocatalysts. *Energy Environ. Sci.* **2020**, *13*, 3361−3392.

(30) Xu, B.; Liu, Z.; Qiu, W.; Liu, Q.; Sun, X.; Cui, G.; Wu, Y.; Xiong, X. La_2O_3 nanoplate: An Efficient Electrocatalyst for Artificial N_2 Fixation to NH_3 with Excellent Selectivity at Ambient Condition. *Electrochim. Acta* **2019**, *298*, 106−111.

(31) Zhang, D.; Song, Y.; Du, Z.; Wang, L.; Li, Y.; Goodenough, J. B. Active $LaNi_{1-x}Fe_xO_3$ Bifunctional Catalysts for Air Cathodes in Alkaline Media. *J. Mater. Chem. A* **2015**, *3*, 9421−9426.

(32) Tong, Y.; Wu, J.; Chen, P.; Liu, H.; Chu, W.; Wu, C.; Xie, Y. Vibronic Superexchange in Double Perovskite Electrocatalyst for Efficient Electrocatalytic Oxygen Evolution. *J. Am. Chem. Soc.* **2018**, *140*, 11165−11169.

(33) Hu, Q.; Yue, B.; Shao, H.; Yang, F.; Wang, J.; Wang, Y.; Liu, J. Facile Syntheses of Perovskite Type $LaMO_3$ (M = Fe, Co, Ni) Nanofibers for High Performance Supercapacitor Electrodes and Lithium-Ion Battery Anodes. *J. Alloys Compd.* **2021**, *852*, No. 157002.

(34) Hwang, J.; Rao, R. R.; Giordano, L.; Katayama, Y.; Yu, Y.; Shao-Horn, Y. Perovskites in Catalysis and Electrocatalysis. *Science* **2017**, *358*, 751−756.

(35) Lai, F.; Feng, J.; Ye, X.; Zong, W.; He, G.; Miao, Y.-E.; Han, X.; Ling, X. Y.; Parkin, I. P.; Pan, B.; Sun, Y.; Liu, T. Energy Level Engineering in Transition-Metal Doped Spinel-Structured Nanosheets for Efficient overall Water Splitting. *J. Mater. Chem. A* **2019**, *7*, 827−833.

(36) Zhao, S.; Berry-Gair, J.; Li, W.; Guan, G.; Yang, M.; Li, J.; Lai, F.; Cora, F.; Holt, K.; Brett, D. J. L.; He, G.; Parkin, I. P. The Role of Phosphate Group in Doped Cobalt Molybdate: Improved Electrocatalytic Hydrogen Evolution Performance. *Adv. Sci.* **2020**, *7*, No. 1903674.

(37) Liu, J.; Kong, X.; Zheng, L.; Guo, X.; Liu, X.; Shui, J. Rare Earth Single-Atom Catalysts for Nitrogen and Carbon Dioxide Reduction. *ACS Nano* **2020**, *14*, 1093−1101.

https://dx.doi.org/10.1021/acsami.1c01510